Understanding the role of four-phonon scattering in the lattice thermal transport of monolayer MoS_2

Saumen Chaudhuri [1,*] Amrita Bhattacharya [2,†] A. K. Das,[1] G. P. Das [3,‡] and B. N. Dev [4,5,§]

[1]*Department of Physics, Indian Institute of Technology Kharagpur, Kharagpur 721302, India*

[2]*Department of Metallurgical Engineering and Materials Science, Indian Institute of Technology Bombay, Mumbai 400076, India*

[3]*Research Institute for Sustainable Energy, TCG Centres for Research and Education in Science and Technology, Sector V, Salt Lake, Kolkata 700091, India*

[4]*Department of Physics and School of Nano Science and Technology, Indian Institute of Technology Kharagpur, Kharagpur, 721302, India*

[5]*Centre for Quantum Engineering, Research and Education, TCG Centres for Research and Education in Science and Technology, Sector V, Salt Lake, Kolkata 700091, India*

(Received 19 March 2024; revised 6 May 2024; accepted 10 May 2024; published 20 June 2024)

In the calculations of lattice thermal conductivity (κ_L), vital contributions stemming from four-phonon scattering is often neglected. The significance of four-phonon scattering in the thermal transport properties of monolayer (ML) MoS_2 has been unraveled using first-principles calculations combined with the Boltzmann transport equation. If only three-phonon scattering processes are considered then the κ_L is found to be significantly overestimated ($\sim$115.8 $W\,m^{-1}\,K^{-1}$ at 300 K). With the incorporation of the four-phonon scattering processes, the κ_L reduces to 24.6 $W\,m^{-1}\,K^{-1}$, which is found to be closer to the experimentally measured κ_L of 34.5 $W\,m^{-1}\,K^{-1}$. Four-phonon scattering significantly impacts the carrier lifetime (τ) of the low-energy out-of-plane acoustic mode (ZA) phonons and thereby, suppresses its contribution in κ_L from 64% (for three-phonon scattering) to 16% (for both three- and four-phonon scatterings). The unusually high four-phonon scattering rate (τ_4^{-1}) of the ZA phonons is attributed to the distinctive quadratic dispersion, along with the combined effects of the acoustic-optical frequency gap, strong anharmonicity, and the selection rule imposed by reflection symmetry. The strong coupling between the dispersion characteristics of the ZA mode and the τ_4^{-1} is discovered through the application of mechanical strain. The strain induced increase in the linearity of the ZA mode dispersion dramatically reduces the significance of the four-phonon scattering in ML-MoS_2, both qualitatively and quantitatively. These findings offer valuable insights into the thermal transport phenomena of ML-MoS_2, as well as other 2D materials.

DOI: 10.1103/PhysRevB.109.235424

I. INTRODUCTION

Monolayer transition metal di-chalcogenides (TMDCs), in the last decade, has attracted immense interest for various practical applications due to its unique physical, chemical and thermal properties [1–3]. Apart from the unique electronic properties, due to the low-dimensional structure and the resulting interface phonon scattering and phonon confinement effects, the two-dimensional (2D) TMDCs come naturally with a low phonon thermal conductivity (κ_L) [as shown in Ref. [4] and references therein]. In the semiconducting TMDCs with a sizable band gap, such as MoS_2, WS_2, HfS_2, ZrS_2 etc., the thermal transport mechanism is almost entirely governed by the lattice contribution (κ_L) to it, and the electronic contribution (κ_e) is found to be negligible [5–7]. Owing to the inverse relationship between $\kappa(=\kappa_L+\kappa_e)$ and thermoelectric efficiency, various 2D TMDCs have emerged as a potential thermoelectric material with considerably high efficiency [5–9]. Alongside experiments, first-principles based calculations have played a significant role in predicting κ_L and thereby, filtering out the best thermoelectric materials [5–9]. However, the accurate prediction of κ_L is extremely important, as an under- or overprediction may lead to misleading conclusions regarding the thermoelectric performance.

Among the various monolayer (ML) TMDCs, the thermal transport properties of MoS_2 has been explored extensively over the years [5,7,10–12]. However, there have been no consensus over the value of κ_L obtained using various theoretical approaches and from experiments. Li *et al.*, using first-principles based calculations combined with the Boltzmann transport equation (BTE), have reported a κ_L of 83 $W\,m^{-1}\,K^{-1}$ for ML-MoS_2 at 300 K with a sample size of 10 μm [13]. The value of κ_L can be further increased by 30% by increasing the sample size. There are multiple theoretical articles based on the first-principles BTE calculations reporting a large κ_L value of ML-MoS_2, such as 116.8 [14], 103 [15] and 131 $W\,m^{-1}\,K^{-1}$ [16]. In fact, the in-plane value of κ_L for bulk-MoS_2 is also found to be as high as 98.9 $W\,m^{-1}\,K^{-1}$ [16]. However, Yan *et al.* measured the thermal conductivity of free-standing single-layer MoS_2 to be only 34.5 $W\,m^{-1}\,K^{-1}$ using temperature dependent Raman spectroscopy [17]. Also, Sahoo *et al.* reported a value of 52 $W\,m^{-1}\,K^{-1}$ measured on a substrate-supported

*Present address: Department of Metallurgical Engineering and Materials Science, IIT Bombay, Mumbai 400076, India.

†Corresponding author: b_amrita@iitb.ac.in

‡Corresponding author: gourpdas@gmail.com

§Corresponding author: bhupen.dev@gmail.com

TABLE I. Lattice thermal conductivity (κ_L) of ML-MoS_2 obtained in this work and from different approximations at room temperature (300 K).

Reference	Method	κ_L (W m^{-1} K^{-1})
This work	DFT: three-phonon (RTA)	115.8
Ref. [17]	Experiment: monolayer	34.5
Ref. [18]	Experiment: few-layer	52
Ref. [14]	DFT: three-phonon (RTA)	116.8
Ref. [16]	DFT: three-phonon (RTA)	131
Ref. [19]	MD	38.1
Ref. [20]	MD	26.2
Ref. [22]	DFPT + NEGF	23.2
This work	DFT: three-phonon (RTA) + four-phonon (RTA)	24.6
This work	DFT: three-phonon (IS) + four-phonon (RTA)	27.7

few-layer MoS_2 film [18]. Compared to the first-principles based calculations on ML-MoS_2, the molecular dynamics (MD) simulations are seen to produce results that are in better agreement with experiments: 38.1 [19], 26.2 [20], and 19.76 W m^{-1} K^{-1} [21]. Besides, Cai *et al.* obtained a value of 23.2 W m^{-1} K^{-1} at room temperature using the combination of density functional perturbation theory (DFPT) and nonequilibrium Green's functions (NEGF) approach [22]. The classical MD simulation results, although ignores the quantum effects in specific heat and phonon scattering, can be considered as a reliable benchmark at 300 K since the Debye temperature of ML-MoS_2 is only ≈ 262 K [23]. Thus, the large discrepancy between the first-principles BTE based calculations and experimentally measured κ_L poses a serious question regarding the reliability of the existing first-principles calculations. Apart from the quantitative disagreement amongst the results (see Table I), the description of the role of individual phonon modes in the thermal transport mechanism of ML-MoS_2 is also baffling. Therefore it is necessary to investigate the thermal transport properties of ML-MoS_2 in greater detail and with better accuracy through systematic first-principle calculations.

Over the years, the density functional theory (DFT) based thermal conductivity (κ_L) calculations have garnered significant popularity due to two reasons: less computational expense and reasonably good agreement with experimental κ_L for variety of systems. To mitigate the computational burden, these calculations consider only the lowest-order intrinsic phonon scattering events involving three phonons. Despite neglecting all the higher-order perturbative anharmonic terms of the crystal Hamiltonian, the first-principles calculations have proved to be reasonably accurate in predicting the κ_L of different materials [24–27]. However, recently, the methodology has come under question, as first-principles DFT based calculations have resulted in the overestimation of thermal conductivity in several materials [28–32], including ML-MoS_2 [14–16]. The subsequent incorporation of the next higher-order anharmonic term, which corresponds to scattering processes involving four phonons, significantly reduces the error in the estimation of κ_L for diamond [28], zinc-blende BAs [29], AlSb [31], and ML-TaS_2 [32]. For graphene, strikingly high four-phonon scattering rate is found, which is even comparable to the three-phonon scattering rate [30]. The inclusion of four-phonon scattering in graphene reduces the relative contribution of the out-of-plane acoustic phonon mode (ZA) in κ_L from 70% to 30%. In case of ML-MoS_2, the better agreement between the κ_L obtained from MD simulations and the experimental data, and the fact that, MD calculations consider all possible orders of phonon scattering events, suggests the potential importance of higher-order anharmonic terms. Therefore it is imperative to incorporate the higher-order phonon scattering processes into the first-principles calculations to understand the thermal transport properties of ML-MoS_2 accurately.

In earlier studies, certain geometrical and phonon characteristics are identified as the governing conditions behind the significantly high four-phonon scattering strength. Examples are, acoustic-optical (a-o) frequency gap in BAs [29], strong anharmonicity in Lennard-Jones argon [28], and mirror reflection symmetry in graphene [30]. The presence of reflection symmetry in 2D materials imposes a unique selection rule, namely reflection symmetry selection rule (RSSR), on the phonon scattering events, i.e., for all orders of phonon-phonon scattering, processes that involve an odd number of out-of-plane phonons (flexural) are forbidden [33]. Therefore three-phonon processes may involve zero or two flexural phonons, while the four-phonon processes may include zero, two or four flexural phonons. In graphene, the RSSR is found to play a decisive role in significantly reducing the relative contribution of the ZA phonons in κ_L [30]. Apart from the identified conditions, the quadratic dispersion of the ZA mode, and the resulting large low-frequency phonon population in 2D materials, is expected to play a significant role behind the high four-phonon scattering strength in single-layer graphene and TaS_2 [30,32]. To understand the coupling between the quadratic phonon dispersion and four-phonon scattering strength, the associated quadraticity of the ZA phonon mode needs to be altered. However, the modification in the dispersion of the ZA mode has to be done in such a way that the essential conditions, as noted earlier, are still met. For ML-MoS_2 as well as for ML-ZnO, it is previously reported that with the application of in-plane tensile strain the dispersion of the ZA mode changes from quadratic to linear [34,35]. The modulation in the three- and four-phonon scattering rates with strain, and thereby, with the quadraticity of the ZA branch will provide a clear understanding of the intrinsic phonon scattering mechanism in ML-MoS_2. It is, therefore, interesting to study the three- and four-phonon

scattering processes in ML-MoS_2 as a function of mechanical strain, which is lacking in literature. One such study may reveal the underlying details of how the various geometrical and phonon dispersion features influence the four-phonon scattering processes in any general material as well. The present work, highlighting the importance of four-phonon scattering in the thermal transport mechanism of ML-MoS_2, is aimed at resolving the ambiguity regarding the magnitude of κ_L and unraveling the coupling between the various phonon dispersion characteristics and four-phonon scattering strength.

II. COMPUTATIONAL DETAILS

First-principles calculations have been performed using *ab initio* density functional theory (DFT) as implemented in the Vienna *ab initio* simulation package (VASP) [36,37] together with projector augmented wave (PAW) potentials to account for the electron-ion interactions [38]. The electronic exchange and correlation (XC) interactions are addressed within the generalized gradient approximation (GGA) of Perdew-Burke-Ernzerhof (PBE) [39]. In all calculations, the Brillouin zone (BZ) is sampled using a well-converged Monkhorst-Pack [40] k-point set ($21 \times 21 \times 1$), and a conjugate gradient scheme is employed to optimize the geometries until the forces on each atom are less than 0.01 eV/Å. In the present calculations, in-plane biaxial strain has been applied by isotropically changing the in-plane lattice parameters to a desired value and then, the internal forces acting on each atom is minimized. A vacuum thickness of approximately 20 Å is used to avoid the spurious interaction between the periodic images of the layers.

The phonon dispersion curves are calculated based on the supercell approach using the finite displacement method with an amplitude of 0.015 Å as implemented in the PHONOPY code [41]. To compute the lattice transport properties, the Boltzmann transport equation (BTE) for phonons is solved as implemented in the SHENGBTE code [42]. The second-, third-, and fourth-order interatomic force constants (IFC) are calculated based on the finite-difference supercell method. For the third-order IFC a $6 \times 6 \times 1$ supercell is created and interactions up to the 6th nearest-neighbor (NN) atom are considered using an extension module of SHENGBTE [42]. Similarly, for the fourth-order IFC, a $4 \times 4 \times 1$ supercell is adopted and 3 NN atoms are considered. Well-converged k meshes, together with a strict energy convergence criterion of 10^{-8} eV, are used in all the supercell based calculations. The three- and four-phonon scattering rates have been computed using SHENGBTE [42]. To accurately compute the lattice thermal conductivity, a dense q mesh of $51 \times 51 \times 1$ is used to sample the reciprocal space of the primitive cells.

Combining the first-principles calculations with the semiclassical Boltzmann transport equation (BTE), the lattice thermal conductivity (κ_L) of a material can be calculated as

$$\kappa_L^{xy} = \frac{1}{N_q V}\sum_{\lambda} \hbar\omega_\lambda \frac{\partial n_\lambda^0}{\partial T} v_{\lambda,x} v_{\lambda,y} \tau_\lambda = \frac{1}{N_q V}\sum_{\lambda} c_\lambda v_{\lambda,x} v_{\lambda,y} \tau_\lambda, \tag{1}$$

where $\lambda = (q, j)$ is a particular phonon mode with wave vector q, dispersion branch j, and frequency ω_λ, V is the volume of the Brillouin zone (BZ), N_q corresponds to the total number of q points sampled in the first BZ, n_λ^0 is the Bose-Einstein distribution function associated with the phonon mode λ at a particular temperature T, $v_{\lambda,x}$ is the x component of the phonon group velocity, τ_λ is the carrier lifetime of the λ mode phonons. The term $\hbar\omega_\lambda \frac{\partial n_\lambda^0}{\partial T}$ corresponds to the phonon specific heat of the λ mode. The intrinsic phonon scattering rates (τ_λ^{-1}) and thereby, the carrier lifetime (τ_λ) are computed according to the Fermi's golden rule and the detailed derivation of the formulas can be found elsewhere [28–32]. In this work, both the three- and four-phonon processes are considered in the scattering rate calculations. Thus the total scattering rate corresponding to the phonon mode λ is computed by the Matthiessen's rule [43], given as

$$\frac{1}{\tau_\lambda} = \frac{1}{\tau_{3,\lambda}} + \frac{1}{\tau_{4,\lambda}}, \tag{2}$$

where $\frac{1}{\tau_{3,\lambda}}$ and $\frac{1}{\tau_{4,\lambda}}$ denote the three-phonon and four-phonon scattering rates, respectively. The total scattering rate is, therefore, computed by summing the contributions stemming from all the possible phonon modes.

The phonon BTE in the steady state, describing the balance of the phonon population for a particular mode λ between the phonon diffusion and scattering, is given as

$$v_\lambda \cdot \nabla n_\lambda = \frac{\partial n_\lambda}{\partial t}, \tag{3}$$

where v_λ is the phonon group velocity and n_λ is the phonon occupation number corresponding to the mode λ. Within the framework of relaxation time approximation (RTA), including the three-phonon and four-phonon scattering processes, the scattering term on the right-hand side can be expressed as $\frac{\partial n_\lambda}{\partial t} = \frac{n_\lambda - n_\lambda^0}{\tau_\lambda}$, where n_λ^0 is the equilibrium Bose-Einstein distribution function. Due to the fact that Normal processes (N) contribute indirectly to the thermal resistance by influencing the phonon distribution and consequently, the Umklapp process (U), a direct summation of the N and U scattering rates within the RTA leads to an inaccurate description of the overall thermal transport. Therefore, when N processes are significant as compared to the U processes, an exact solution of the phonon BTE, beyond the RTA, is required. Within the iterative scheme (IS) the phonon BTE is solved by considering all the phonon scattering events simultaneously, as opposed to the RTA where scattering events are treated independent to each other. In the IS, each phonon's initial state is coupled with the final states of all other phonons and thus, the current scattering events can be influenced by the results of all the former scattering events. Therefore the IS, employing the exact solution to the phonon BTE, enables the separation of the thermal conductivity contribution from each phonon branch.

III. RESULTS AND DISCUSSION

A. Pristine monolayer MoS_2

The single-layer counterpart of 2H-MoS_2 consists of a Mo atomic plane sandwiched between two S atomic planes. The unit cell of monolayer MoS_2 in the undistorted 2H phase is composed of a triangular lattice of Mo atoms arranged in a trigonal prismatic structure with the two triangular lattices of S atoms, as shown in Fig. 1. Structural relaxation results in

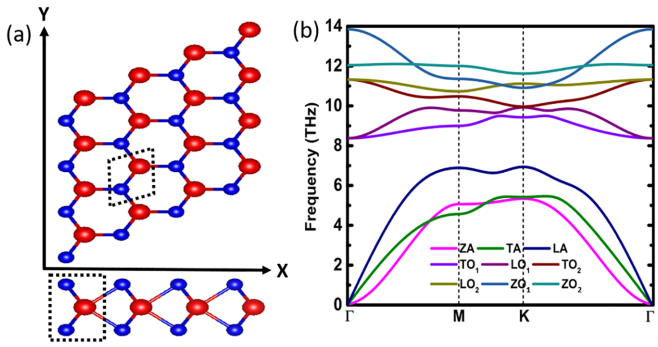

FIG. 1. (a) Crystal structure (top and side view) of monolayer MoS_2, where the Mo and S atoms are shown as red and blue balls, respectively. The black dashed box represents the primitive unit cell. (b) Phonon dispersion of ML-MoS_2 along the high-symmetry path (Γ-M-K-Γ) of the Brillouin zone (BZ).

a lattice parameter of $a = b = 3.18$ Å, consistent with the previous theoretical studies [34,44]. Monolayer (ML) 2H-MoS_2 is a direct band gap semiconductor with a band gap of 1.7 eV [5,34,44]. Therefore the heat conduction through ML-MoS_2 is largely governed by the phonon transport characteristics. From the phonon dispersion of pristine ML-MoS_2, as shown in Fig. 1, certain important characteristics related to the phonon transport and intrinsic phonon-phonon scattering can be immediately identified. For example, the quadratic dispersion of the out-of-plane acoustic mode (ZA) i.e., the flexural mode, which is typical of a 2D material, and the acoustic-optical (a-o) phonon frequency gap of 1.21 THz arising from the mass difference of Mo and S atoms. These characteristics of the phonon dispersion are found to have significant implications over the intrinsic phonon scattering processes in some earlier studies [28–32].

The intrinsic phonon scattering directly impacts the lattice thermal transport properties and therefore, the lattice thermal conductivity (κ_L) can be taken as a measure of the intensity of phonon scattering. Large phonon scattering rates result in a small carrier lifetime (τ) and thereby, lead to a low κ_L. Our calculated κ_L of ML-MoS_2 as a function of temperature (T), considering only three-phonon scattering within the relaxation time approximation (RTA), is presented in Fig. 2. The value of κ_L obtained at 300 K using the relaxation time approximation (RTA) is 115.8 $W\,m^{-1}\,K^{-1}$, which agrees well with earlier first-principles calculations based reports [14–16]. A comparison of the κ_L values of ML-MoS_2 at 300 K obtained from experiments and different theoretical works are provided in Table I. A large discrepancy in the values of κ_L obtained from experiments or MD simulations and first-principles calculations can be seen from Table I and also discussed in the Introduction (Sec. I). This limited accuracy poses serious questions toward the approach used in first-principles calculations. For more insights, the contribution towards the κ_L at 300 K and the Grüneisen parameter (γ) corresponding to the individual phonon modes are calculated (see Fig. 2). It can be seen that the ZA mode contributes the highest to the total κ_L. In contrast, the magnitude of γ associated with the ZA mode is also very high (see Fig. 2), which generally corresponds to strong anharmonicity and therefore implies a high phonon scattering rate (τ^{-1}). In spite of having the highest γ, such a high κ_L corresponding to the ZA phonons is something unusual. The large overestimation of the total thermal conductivity and specifically, the ambiguous description of the role of ZA phonons suggests the inadequacy of the three-phonon based first-principles BTE calculations in predicting the thermal transport properties of ML-MoS_2.

To understand the role of higher order anharmonicity in the phonon scattering and therefore, the transport properties, we calculate the four-phonon scattering rate of ML-MoS_2. The variation in the three- and four-phonon scattering rates of ML-MoS_2 as a function of phonon frequency is calculated at two different temperatures i.e., at 300 and 900 K, and are presented in Fig. 3. It can be seen that, at 300 K the four-phonon scattering rate is comparable and even higher compared to the three-phonon scattering rates at some frequencies (in the low frequency limit). At higher temperatures, such as at 900 K, the four-phonon scattering dominates the overall phonon scattering processes. Such a high four-phonon scattering rate is against the general notion of perturbation theory, which states that the strength of higher-order scattering depends on the magnitude of corresponding higher-order terms of the Hamiltonian, which gets progressively smaller

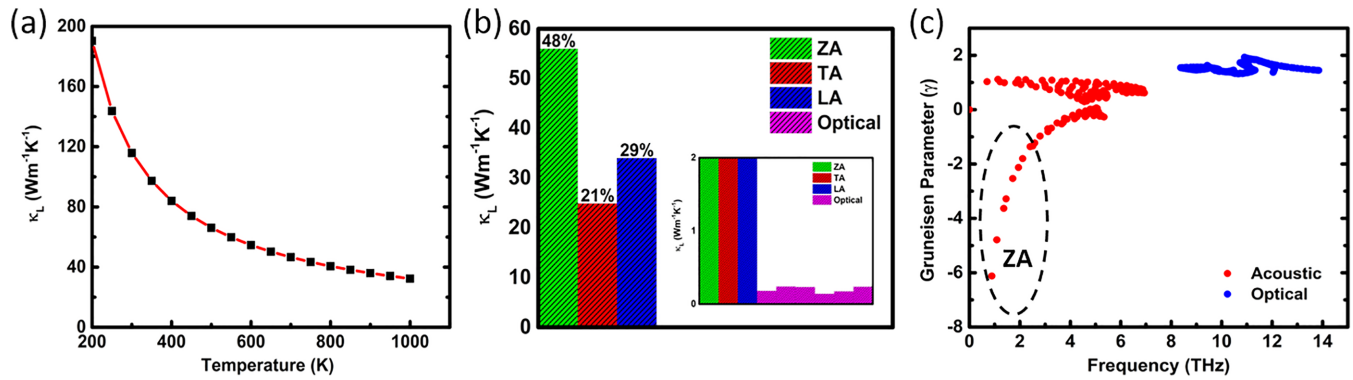

FIG. 2. (a) Variation in lattice thermal conductivity (κ_L) of ML-MoS_2 with temperature considering only three-phonon scattering processes. (b) Contribution to the total κ_L from the individual phonon modes, i.e., the flexural acoustic (ZA), transverse acoustic (TA), longitudinal acoustic (LA) and optical modes at a temperature of 300 K. [(b), inset)] Zoomed in. (c) Variation in the Grüneisen parameter (γ) as a function of phonon frequency. The contribution stemming from the ZA mode is highlighted by the oval circle.

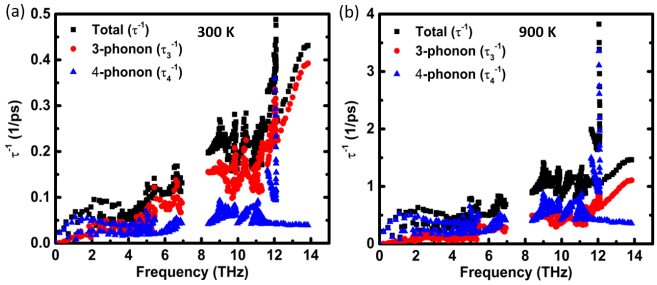

FIG. 3. Variation in the three-phonon (τ_3^{-1}; red dots), four-phonon (τ_4^{-1}; blue dots), and total ($\tau_3^{-1} + \tau_4^{-1}$; black dots) scattering rates of ML-MoS_2 with phonon frequency at (a) 300 and (b) 900 K.

with the order number. Feng *et al.* have demonstrated a similar phenomenon in a number of materials [28–31]. Notably, in the low frequency regime, such as 0–2 THz, the four-phonon scattering rate is astonishingly high and the three-phonon scattering rate is negligible. This can be correlated with the unique quadratic dispersion of the flexural (ZA) phonons near the zone center (Γ). In the frequency range of 0–2 THz, the ZA phonons have the highest population density owing to the quadratic dispersion and therefore, the corresponding scattering phase space is also high.

The low three-phonon scattering rates of the ZA phonons can be understood from the simultaneous effect of a-o frequency gap and the RSSR. Owing to the horizontal mirror reflection symmetry of ML-MoS_2, of which the mirror plane is in the Mo atomic plane, the RSSR is relevant to all orders of phonon scattering processes. In graphene, This unique phenomenon is found to forbid a significant number of three-phonon scattering processes involving the ZA phonons and thereby, resulting in a large overestimation of the κ_L associated with it [30]. Even in a quasi-two-dimensional material like diamane, the horizontal reflection symmetry is found to strongly influence the intrinsic phonon scattering rates [45]. Due to the large a-o frequency gap, a large number of three-phonon processes involving low-lying ZA phonons and high energy optical phonons are restricted, as dictated by the energy conservation criteria (ECC). This, coupled with the RSSR, which prohibits scattering events involving an odd number of ZA phonons, such as aoo, aaa etc., results in an ultra-high lifetime (τ) for the ZA phonons. However, in the case of four-phonon scattering events, the additional phonon allows for the acoustic-optical gap to be overcome, thereby strengthening the coupling between acoustic and optical phonons. Also, the RSSR allows zero, two or four out-of-plane phonons to take part in the four-phonon scattering events, while only combinations of zero and two phonons are allowed in a three-phonon process. Therefore the scattering phase space of the ZA phonons in three-phonon processes is much smaller as compared to that of the four-phonon processes, which results in the superiority of the four-phonon scattering rates in the low frequency range.

To get further insight of the scattering processes, we calculate the scattering rates corresponding to every possible way of scattering allowed in both the three- and four-phonon processes. There are two possibilities in a scattering process involving three phonons, such as, a single phonon may split

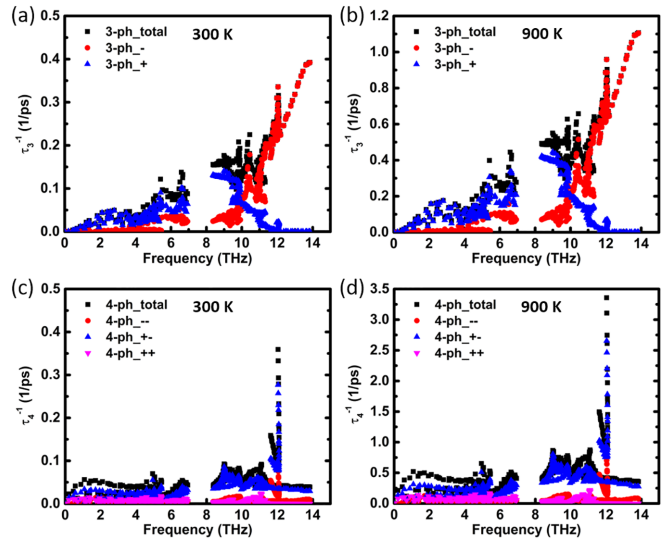

FIG. 4. Variation in the scattering rates corresponding to the [(a) and (b)] three-phonon and [(c) and (d)] four-phonon scattering processes at 300 and 900 K. The three-phonon scattering processes are denoted as; "+": combination, where two phonons combine to form one new phonon and '–": splitting, where one phonon splits into two phonons. The four-phonon scattering events are denoted as; "++": combination, where three phonons combine to form a single phonon, "−−": splitting, where one phonon splits into three phonons and "+−": redistribution, where two phonons scatter to generate two new phonons.

into two phonons (splitting, −), or two phonons may combine to create a new phonon (combination, +). Similarly, four phonons may engage in three possible ways, such as, a single phonon may split into three phonons (splitting, −−), or three phonons may combine to form a new phonon (combination, ++), or two phonons may combine to create two new phonons (redistribution, +−). The variation in the scattering rates corresponding to all the possible channels of three- and four-phonon processes at temperatures 300 and 900 K are presented in Fig. 4. For the three-phonon processes, in the low energy region (0–7 THz) the three phonon combination (+) is favorable, while in the high energy region (8-14 THz) the splitting (-) is dominant. This can be understood as a consequence of the ECC. For the four-phonon processes, on the other hand, the four phonon redistribution (+−) is found to be the dominant one in the entire frequency range. Due to the nearly dispersionless character of the ZO_2 mode at a frequency around 12 THz, the four-phonon scattering, albeit mainly the four phonon redistribution process (+−) peaks.

From Figs. 3 and 4, it becomes evident that while four-phonon scattering is significant at room temperature, its importance increases considerably at higher temperatures. To understand the superiority of the four-phonon scattering at high temperatures, we calculate the temperature dependency of the three- and four-phonon scattering rates corresponding to all the nine phonon modes at a particular q point (0.15, 0, 0) of the BZ, as shown in Fig. 5. It can be seen that, while τ_3^{-1} increases linearly with temperature, τ_4^{-1} increases quadratically, for all the phonon modes. These temperature dependencies follow from the fact that, at a particular temperature τ_3^{-1}

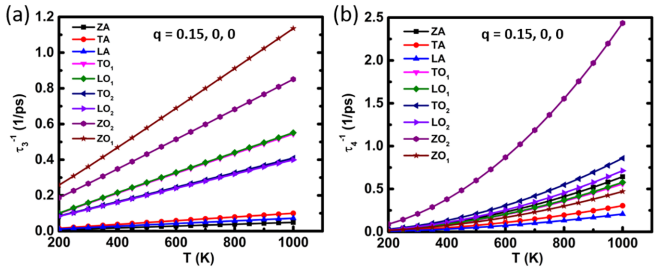

FIG. 5. (a) three-phonon and (b) four-phonon scattering rates plotted as a function of temperature corresponding to all the phonon modes of ML-MoS_2. The scattering rates are calculated at a particular q point (0.15, 0, 0) of the BZ located between Γ and M points.

is proportional to the phonon population, whereas the τ_4^{-1} depends on the square of the population, and the phonon population scales linearly with temperature. Such scaling laws of the scattering rates have been seen in earlier reports [28,29] as well, suggesting the validity of our phonon scattering calculations. From Fig. 5, it is clear that the τ_3^{-1} and τ_4^{-1} associated with the optical modes are the highest and therefore, their contribution towards the thermal transport is significantly less compared to the acoustic modes. Amongst the three acoustic modes, the ZA mode is found to have the lowest values of τ_3^{-1} in the entire temperature range [see Fig. 5(a)]. However, the τ_4^{-1} corresponding to the ZA mode is remarkably high compared to the other two acoustic modes, and even higher compared to some of the optical modes. The highest values of τ_4^{-1}, observed at all temperatures, correspond to the ZO_2 mode due to its nearly flat bandstructure and resulting high availability of phononic states, as has been discussed earlier. To further support the above conclusions, the calculation has been repeated at another q point (0.3, 0, 0) and similar phenomena is observed, as can be seen in Fig. S1 (see Ref. [46]).

To understand the phonon scattering mechanism of the acoustic modes in detail, we calculate the τ_3^{-1} and τ_4^{-1} with respect to the reduced wave vector along a specific q path (Γ-M) of the BZ for the three acoustic modes (ZA, LA, and TA) at temperatures 300 and 900 K, as presented in Fig. 6. We chose to calculate the scattering rates only for the acoustic modes, as the thermal transport properties of ML-MoS_2 are almost entirely governed by the acoustic modes. It can be seen that at $T = 300$ K, except the ZA mode, for the other two acoustic modes τ_3^{-1} is higher than the τ_4^{-1} throughout the q path (Γ-M), which is aligned with the general notion following the perturbation theory. However, for the ZA mode, the τ_4^{-1} is well above τ_3^{-1} for all q points in the high-symmetry path Γ-M. The difference, τ_4^{-1} - τ_3^{-1}, is large for q points near the zone center (Γ-point), which corresponds to the low frequency region. At higher temperatures, such as 900 K, due to the quadratic dependency of τ_4^{-1} on temperature, the four-phonon

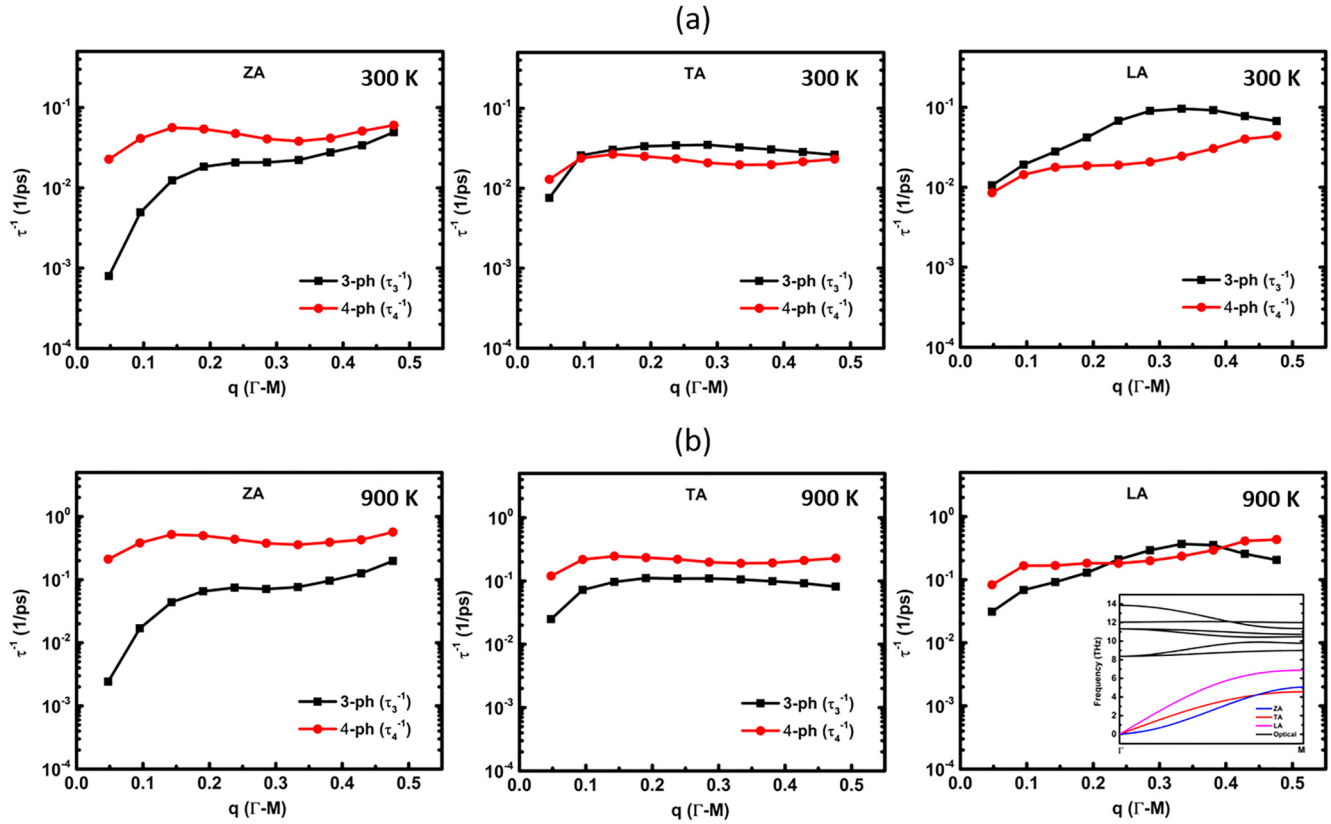

FIG. 6. Variation in three-phonon (τ_3^{-1}) and four-phonon (τ_4^{-1}) scattering rates corresponding to the three acoustic modes (ZA, TA, and LA) plotted as a function of the reduced wave vector along the high-symmetry q path of Γ-M at a temperature of (a) 300 and (b) 900 K. The x coordinate of 0.0 corresponds to the Γ point and 0.5 corresponds to the M point of the BZ. The phonon dispersion of ML-MoS_2 from Γ to M is shown in inset.

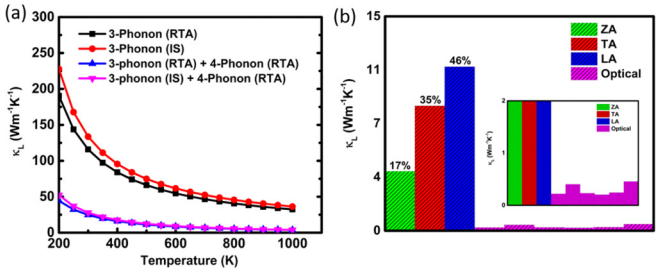

FIG. 7. (a) Variation in the lattice thermal conductivity (κ_L) of ML-MoS_2 plotted as a function of temperature. The plot includes results obtained with and without the incorporation of four-phonon scattering processes using RTA and IS. (b) Contribution in κ_L from the individual phonon modes at 300 K using both three- and four-phonon scattering rates. [(b), inset] Zoomed in.

processes dominate and τ_4^{-1} becomes higher than τ_3^{-1} for all three acoustic modes. The scattering rates corresponding to the possible channels involving three phonons $(+, -)$ and four phonons $(++, +-, --)$ as a function of the wave vector along Γ-M is provided in Figs. S2 and S3 (see Ref. [46]). It is found that, while the combination $(+)$ process dominates the three-phonon processes, the four-phonon processes are dominated by the redistribution $(+-)$ process.

To understand the importance of four-phonon scattering in the thermal transport properties of ML-MoS_2, we calculate the lattice thermal conductivity: $\kappa_{L(3)}$ and $\kappa_{L(3+4)}$ based on the RTA solved τ_3^{-1} and $\tau_3^{-1} + \tau_4^{-1}$, respectively. The variation in $\kappa_{L(3)}$ and $\kappa_{L(3+4)}$ of ML-MoS_2 as a function of temperature is shown in Fig. 7. We find that the inclusion of four-phonon scattering into the thermal transport calculations significantly reduces the thermal conductivity from 115.8 to 24.6 $W\,m^{-1}\,K^{-1}$ at the temperature of 300 K. Our result of $\kappa_{L(3+4)}$ agrees well with previously reported experimental values and also with the predictions based on MD simulations [17–22]. The $\kappa_{L(3)}$ computed by accounting only the three-phonon scattering seems to significantly overestimate the thermal conductivity, as the subsequent incorporation of four-phonon scattering leads to reductions at all temperatures. It is, therefore, clear that the four-phonon processes have a compelling role in governing the thermal transport properties of ML-MoS_2 at all temperatures. To understand the impact of the four-phonon scattering in greater detail, we calculate the contribution of each phonon mode in $\kappa_{L(3+4)}$, as presented in Fig. 7. The reduction in κ_L, following the inclusion of four-phonon scattering, mainly comes from the ZA branch, whose contribution in κ_L reduces from ≈64% to ≈16%. The restricted three-phonon phase space of the ZA mode, resulting from the a-o frequency gap and RSSR, leads to a remarkably high τ and thereby, a largely overestimated $\kappa_{L(3)}$. The large τ_4^{-1} corresponding to the ZA mode suppresses its contribution in $\kappa_{L(3+4)}$ to a value lower than the other two acoustic modes. The contribution from the optical modes in heat transport remain insignificant even after the incorporation of four-phonon scattering.

Additionally, we observed that our result of $\kappa_{L(3+4)}$ (24.6 $W\,m^{-1}\,K^{-1}$) using the relaxation time approximation (RTA) is less than the experimentally measured value. This is something unusual, as in experiments, a phonon can scatter from various sources apart from another phonon, such as defects, grain boundaries, etc., depending on the material parameters. The underprediction in the values of $\kappa_{L(3+4)}$ stems from the fact that, in RTA calculations, both the Normal (N) and Umklapp (U) processes are regarded as sources of direct thermal resistance. However, only the U processes can introduce thermal resistance directly, whereas the N processes are generally considered as nonresistive. Therefore RTA based calculations can produce accurate prediction of κ_L only for those materials where N processes are negligible. It can be seen from Fig. S4 (see Ref. [46]) that, in case of ML-MoS_2, N processes dominate the overall four-phonon scattering, similar to graphene [30]. From the variation of the scattering rates corresponding to the N and U processes as a function of the wave vector along Γ-M (see Fig. S5 in Ref. [46]), it is clear that U processes dominate only around the BZ edge. Therefore appropriate handling of the N and U processes, beyond the RTA, is important for the accurate prediction of κ_L. Thus, we have calculated the κ_L using the IS by solving the BTE for the three-phonon interactions iteratively. However, due to the high computational cost, the four-phonon scattering rates are calculated within the RTA level only and inserted into the iterative scheme. Similar approach has already been used in earlier reports [28,29]. Due to the accurate treatment of N processes as nonresistive, calculations based on the IS predict higher values of κ_L compared to the RTA. For example, the three-phonon based $\kappa_{L(3)}$ of ML-MoS_2 at 300 K calculated using the IS is found to be 133.5 $W\,m^{-1}\,K^{-1}$ compared to the 115.8 $W\,m^{-1}\,K^{-1}$ obtained using the RTA solution, as can be seen from Fig. 7(a). Similarly, the IS solved $\kappa_{L(3+4)}$ of ML-MoS_2 at 300 K is found to be 27.7 $W\,m^{-1}\,K^{-1}$, which is even more closer to the experimentally found κ_L than the RTA predicted one. We, therefore, conjecture that the best accurate values of κ_L of ML-MoS_2 can be found if the four-phonon processes are incorporated within the iterative scheme too. However, the substantial reduction in error in predicting the experimental lattice thermal conductivity, i.e., from 230% error using only $\kappa_{L(3)}$ to only 20% error with $\kappa_{L(3+4)}$, underscores the significance of four-phonon scattering in ML-MoS_2. A table containing the values of κ_L at 300 K using different level of approximations is presented in Table I.

B. Strain induced modifications

To get an in-depth understanding of the role of certain geometrical and phonon dispersion characteristics, such as the a-o frequency gap, RSSR, quadratic dispersion of the ZA phonon branch, and reflection symmetry, in governing the intensity of four-phonon scattering, we applied in-plane biaxial tensile strain on ML-MoS_2. The phonon dispersion, density of states (DOS) and the Grüneisen parameter (γ) of ML-MoS_2 under 8% biaxial tensile strain (BI_8), along with those in the unstrained condition (BI_0), are shown in Fig. 8. Certain changes in the phonon dispersion characteristics, induced by the in-plane tensile strain, can be immediately noticed from Fig. 8. The application of strain induces blue shift in the optical phonon modes and softens the LA and TA modes, which results from the weakening of the Mo-S bond strength. However, the a-o frequency gap remains nearly unchanged:

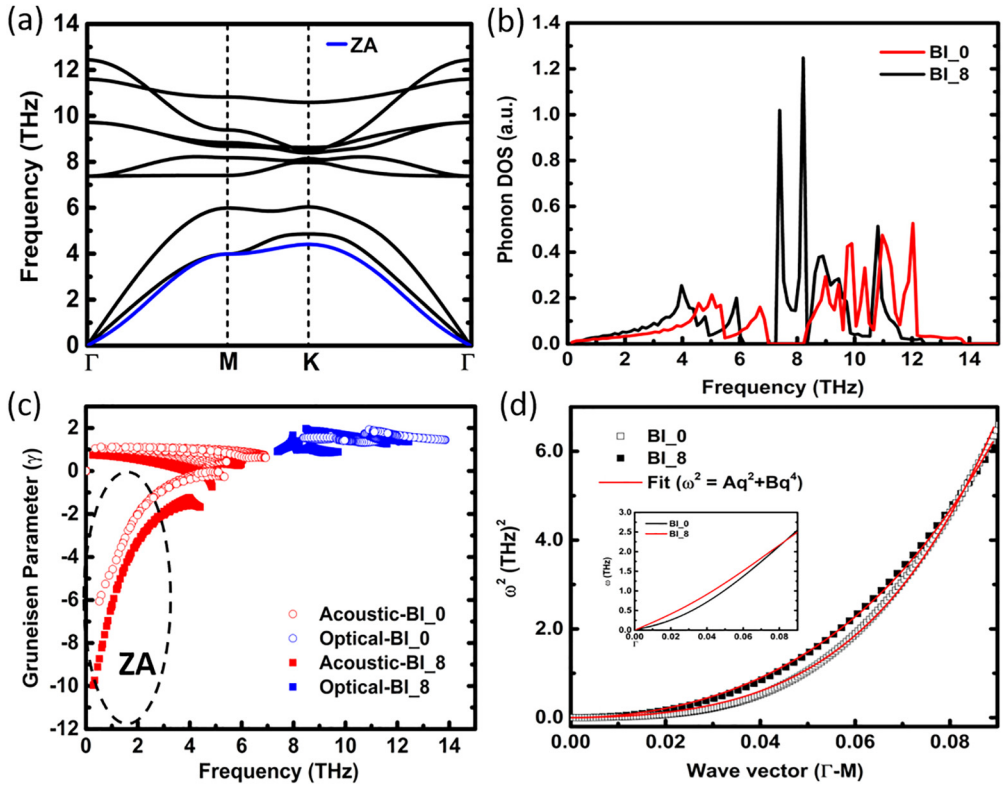

FIG. 8. (a) The phonon dispersion of ML-MoS_2 under 8% biaxial tensile strain. The ZA phonon branch is highlighted in blue. Variation in the (b) phonon density of states (DOS) and (c) Grüneisen parameter (γ) as a function of phonon frequency in the unstrained (BI_0) and 8% biaxially strained (BI_8) condition. (d) Plot of ω^2 as a function of the wave vector (q) around the Γ point along the q path Γ-M along with the fitting function $\omega^2 = Aq^2 + Bq^4$. (Inset) ZA phonon mode dispersion close to the Γ point of the BZ for the unstrained (BI_0) and the 8% biaxially strained (BI_8) ML-MoS_2.

1.21 THz in the unstrained condition and 1.15 THz in the 8% biaxial strained case (BI_8), as also can be seen from the phonon DOS in Fig. 8. With the application of strain, the bond anharmonicity associated with MoS_2 increases, as can be seen from the increase in the magnitude of Grüneisen parameter (γ) in the low frequency limit [see Fig. 8(c)]. The enhancement in the γ, especially in the low frequency region (0–2 THz), clearly indicates an enhanced scattering of the acoustic phonons. Additionally, the application of isotropic in-plane biaxial strain does not alter the hexagonal crystal symmetry of ML-MoS_2, and therefore, the RSSR, which is an outcome of the mirror reflection symmetry, is still valid in the strained condition. Apart from that, the application of strain lowers the quadraticity of the ZA phonon mode and thereby, turns the ZA mode dispersion into a nearly linear one in the 8% biaxially strained condition. To quantify the change in the quadraticity, we fitted the dispersion of the ZA mode near the BZ center (Γ point) along the Γ-M path with a model equation $\omega^2 = Aq^2 + Bq^4$, where ω is the frequency of the ZA mode at a wave vector q (see Fig. 8). The coefficients A and B are related to the linear and quadratic character of the dispersion, respectively. From the fitting, the values of A and B obtained in the unstrained condition are 260 $m^2\,s^{-2}$ and 70 402 $m^4\,s^{-2}$, whereas in the strained condition the values become 505 $m^2\,s^{-2}$ and 35 037 $m^4\,s^{-2}$. It is, therefore clear that, with strain application, the linear character increases and the quadratic character decreases in the dispersion of the ZA mode.

From the above discussion, it is evident that the features responsible for the unusually high four-phonon scattering in the unstrained condition, such as the acoustic-optical frequency gap, RSSR, and strong anharmonicity, remain present in the strained condition. It is, therefore, legitimate to expect a similar dominance of the four-phonon scattering over the thermal transport properties of ML-MoS_2 in the strained condition. However, in the strained case, the τ_4^{-1} is found to be negligible compared to the τ_3^{-1} at 300 K, and even at higher temperatures, such as 900 K, it remains insignificant. The variation in the phonon scattering rates as a function of frequency at temperatures 300 and 900 K under 8% biaxial tensile strain (BI_8) are presented in Fig. 9. It can be seen that, even in the low frequency region (0–2 THz), the scattering strength corresponding to the four-phonon process is inconsequential. In the unstrained condition, on the other hand, the τ_4^{-1}/τ_3^{-1} was found to be the highest in the same low frequency region (0–2 THz). The small τ_4^{-1} in the strained condition, despite meeting all the conditions for strong four-phonon scattering, is surprising and therefore, needs a detailed investigation. The scattering rates corresponding to all possible three-phonon (+, −) and four-phonon (++, +−, −−) processes are computed as a function of the phonon frequency, and shown in Fig. S6 (see Ref. [46]). Similar to the unstrained condition,

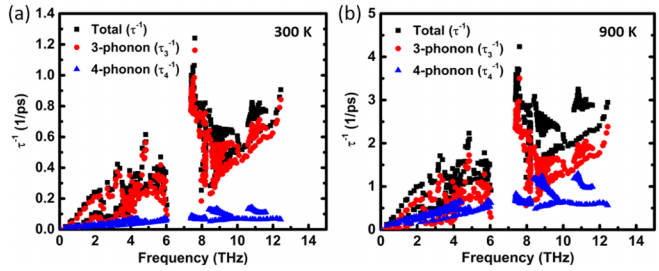

FIG. 9. The three-phonon (τ_3^{-1}; red dots), four-phonon (τ_4^{-1}; blue dots), and total ($\tau_3^{-1} + \tau_4^{-1}$; black dots) scattering rates of ML-MoS_2 in the strained condition (BI_8) at temperatures (a) 300 and (b) 900 K.

the combination process (+) is found to dominate the three-phonon processes in the low frequency region, and splitting process (−) in the high frequency region. Similarly, for the four-phonon processes, the redistribution process (+−) is observed to dominate in the entire frequency range. It is, therefore, clear that the scattering mechanisms involving three or four phonons are identical in both unstrained and strained cases.

The variation in the τ_3^{-1} and τ_4^{-1} with temperature in a range of 200 to 1000 K at a particular q point ($q = 0.15, 0, 0$) of the BZ are shown in Fig. 10. It is evident that the overall scattering rate increases with the application of strain, owing to the increase in Grüneisen parameter (γ) and the resulting increase in anharmonicity. The magnitude of τ_3^{-1}, averaged for all the modes, increases ≈ 2 times in the strained condition (BI_8) compared to that of the unstrained one (BI_0) at nearly all temperatures. However, the impact of strain on the mode-averaged τ_4^{-1} is much less pronounced compared to that of the τ_3^{-1}. The scattering rates corresponding to the optical modes are much higher compared to the acoustic modes for both three- and four-phonon processes at all temperatures. Therefore the role of the optical modes in the lattice thermal transport is insignificant even in the strained case. Amongst the three acoustic modes, the ZA mode, which had the lowest τ_3^{-1} associated with it in the unstrained case, has now the highest τ_3^{-1} in the strained condition. Unlike the unstrained case, the τ_4^{-1} corresponding to the three acoustic modes (ZA, TA and LA) are nearly equal in the strained condition (BI_8).

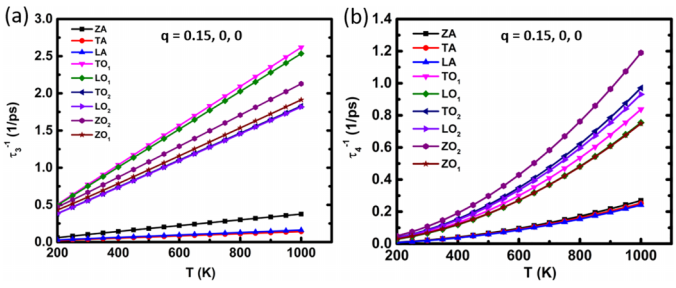

FIG. 10. (a) Three-phonon and (b) four-phonon scattering rates plotted as a function of temperature for different phonon modes in ML-MoS_2 in the 8% biaxially strained condition (BI_8). The scattering rates are calculated at a particular q point (0.15, 0, 0) of the BZ located between Γ and M points.

Thereby, the τ_4^{-1} associated with the ZA phonons is surprisingly low as compared to the unstrained case (BI_0) in the entire temperature range.

To gain further insights into the intrinsic phonon scattering processes in the strained ML-MoS_2, we calculate the τ_3^{-1} and τ_4^{-1} of the acoustic modes along the q path Γ-M, similar to what has been done in the unstrained case. The variation in the scattering rates as a function of the reduced wave vector along Γ-M is presented in Fig. 11. In contrast to the unstrained condition, we observe that for all three acoustic modes (ZA, TA, and LA) along the q path Γ-M at 300 K, the τ_3^{-1} is higher than the τ_4^{-1}. Additionally, the ZA mode exhibits the highest values of the relative strength of three-phonon scattering (τ_3^{-1}/τ_4^{-1}). In summary, among the three acoustic modes, while the room temperature τ_3^{-1} is lowest and τ_4^{-1} is highest for the ZA mode in the unstrained condition, the opposite is observed in the strained case, i.e., τ_3^{-1} is highest and τ_4^{-1} is lowest. Even at a high temperature of 900 K, despite the quadratic temperature dependency of τ_4^{-1}, the τ_3^{-1} corresponding to the ZA mode can be seen to have higher values compared to the τ_4^{-1} [see Fig. 11(b)]. On the contrary, at 900 K, the τ_4^{-1} of the ZA phonons has been found to be significantly higher compared to the τ_3^{-1} in the unstrained condition. The variation in the scattering rates (τ_3^{-1} and τ_4^{-1}) of the acoustic modes corresponding to all the possible processes involving three (+, −) or four (++, +−, −−) phonons along the q path Γ-M are shown in Figs. S7 and S8 (see Ref. [46]). Similar results to what have been observed in Figs. S2 and S3 are seen.

Finally, the calculated phonon scattering rates are incorporated to compute the lattice thermal conductivity (κ_L) of ML-MoS_2 in the biaxial 8% strained condition (BI_8). The variation in $\kappa_{L(3)}$ and $\kappa_{L(3+4)}$, based on τ_3^{-1} and $\tau_3^{-1} + \tau_4^{-1}$, respectively, as a function of temperature are presented in Fig. 12. The values of $\kappa_{L(3)}$ and $\kappa_{L(3+4)}$ at 300 K are found to be 21.6 and 12.2 $W\,m^{-1}\,K^{-1}$, respectively. Compared to the ∼80% reduction in κ_L in the unstrained case, the inclusion of the four-phonon scattering brings only ∼40% reduction in the strained case. Hence, it is evident that due to the low values of τ_4^{-1}, the significance of four-phonon scattering is substantially lower in the strained case compared to the unstrained one. From the plot illustrating the contribution of individual phonon modes to the total κ_L, it is evident that, apart from the optical modes, the lowest contribution comes from the ZA mode [see Fig. 12(b)]. The results remain consistent even after the inclusion of four-phonon scatterings, with only quantitative changes observed. The ZA phonons, having the highest magnitudes of the Grüneisen parameter (γ), exhibiting the lowest values of κ_L, agrees well with the general notion. The accurate description of the qualitative role of ZA phonons in thermal conduction, considering only three-phonon scattering, demonstrates the diminished importance of four-phonon scattering with strain. To comprehend the necessity to go beyond the RTA solution, we have computed the τ_4^{-1} corresponding to the Normal (N) and Umklapp (U) processes for the 8% strained MoS_2. The variation in the τ_4^{-1} associated with the N and U processes as a function of the phonon frequency is shown in Fig. S9, and as a function of the wave vector along the q path Γ-M is presented in Fig. S10 (see Ref. [46]). It is evident that even in the strained condition,

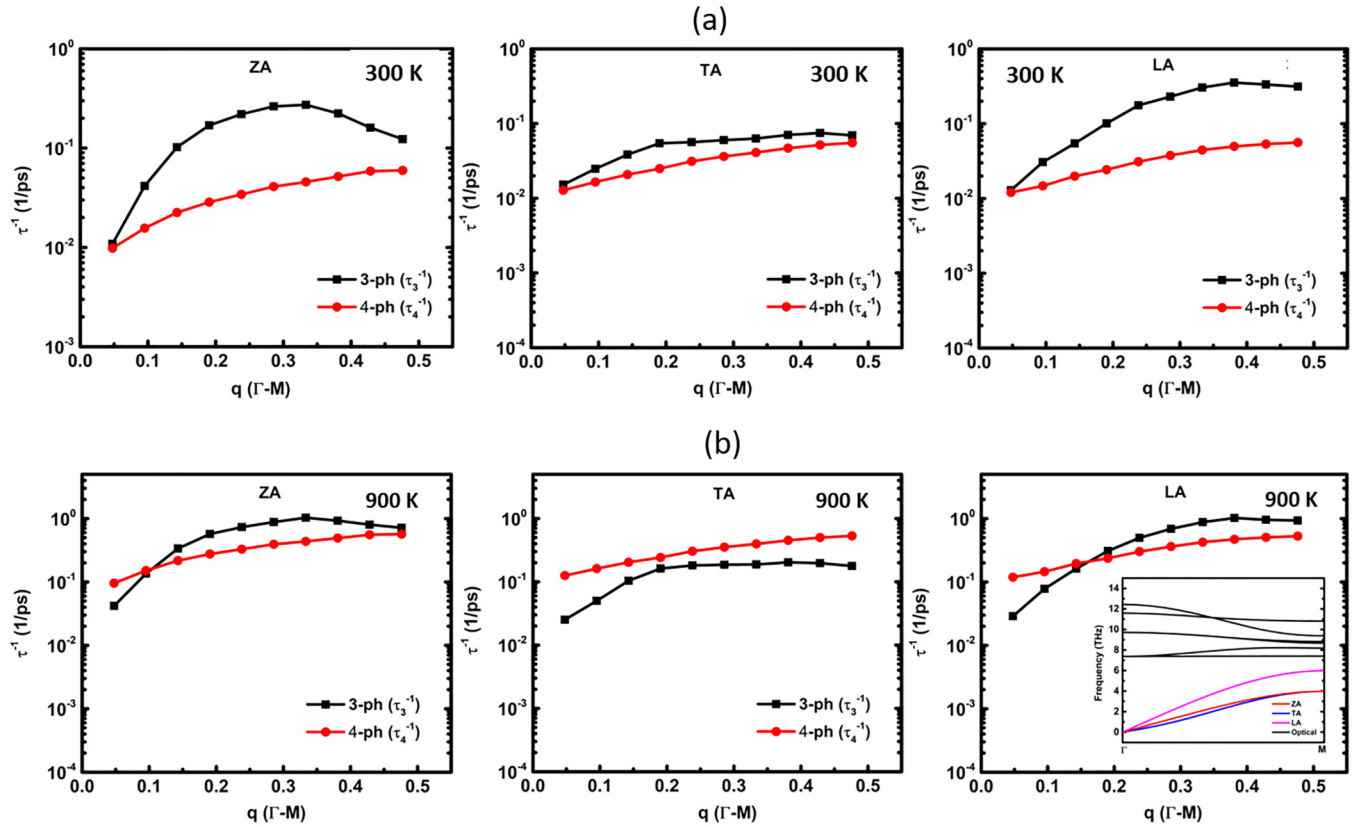

FIG. 11. Variation in three-phonon (τ_3^{-1}) and four-phonon (τ_4^{-1}) scattering rates corresponding to the three acoustic modes (ZA, TA, and LA) of ML-MoS_2 in the strained condition as a function of the reduced wave vector along the q path Γ-M at temperatures (a) 300 and (b) 900 K. The phonon dispersion for 8% biaxially strained ML-MoS_2 along Γ-M is shown in inset.

the relative strength of the N processes remain significant compared to that of the U processes. Therefore the IS must be employed in the strained case as well to achieve better accuracy. Similar to the unstrained case, solving the four-phonon scattering within the RTA level and inserting them into the IS, the values of $\kappa_{L(3)}$ and $\kappa_{L(3+4)}$ at 300 K are found to be 26.3 and 15.7 $W\,m^{-1}\,K^{-1}$, respectively. Thus, by incorporating both three- and four-phonon scattering, we predict a ≈43% reduction in κ_L of ML-MoS_2 with the application of 8% in-plane biaxial tensile strain. This prediction is significantly lower compared to the prediction of ≈82% reduction using three-phonon scattering only. In the absence of experimental validation for the thermal conductivity of ML-MoS_2 in the strained condition, results from the MD studies can be considered as a reliable benchmark. The prediction of a 43% reduction in κ_L with 8% biaxial strain, obtained when both the three-phonon and four-phonon scattering is considered,

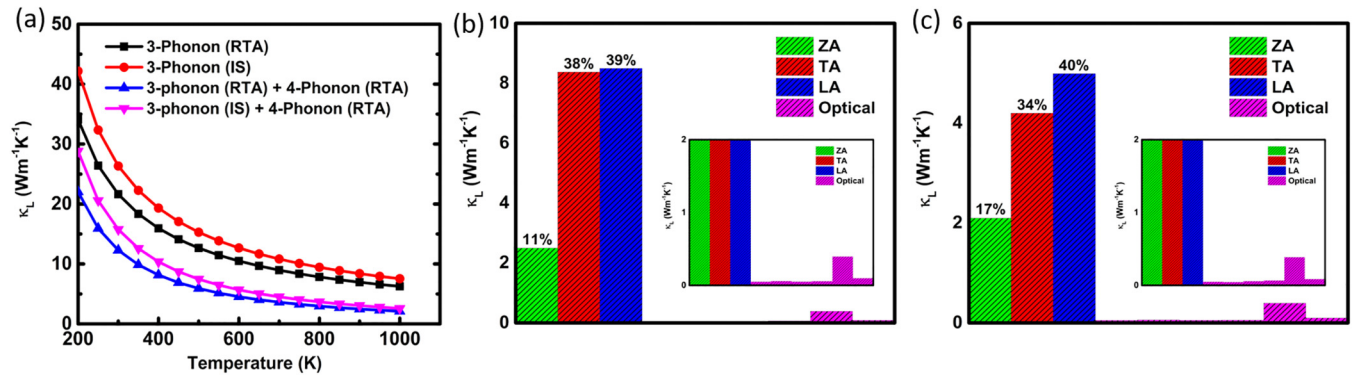

FIG. 12. (a) Variation in the κ_L of ML-MoS_2 plotted as a function of temperature in the 8% biaxially strained condition (BI_8). The plot includes results obtained with and without incorporating the four-phonon scattering using RTA and IS. Contribution in the κ_L of strained ML-MoS_2 (BI_8) at 300 K from the individual phonon modes considering (b) three-phonons only and (c) both three-phonon and four-phonon scattering rates. [(b) and (c), inset] Zoomed in.

aligns well with the MD calculation based prediction of a 60% reduction with 12% uniaxial strain [47].

Despite meeting the necessary conditions, such as the a-o frequency gap, reflection symmetry, and strong anharmonicity, for large four-phonon scattering strength, ML-MoS_2 in the strained condition (BI_8) exhibits a relatively lower four-phonon scattering rate. Among the three acoustic modes (ZA, TA, and LA), the ZA phonons exhibit the lowest relative strength of four-phonon scattering (τ_4^{-1}/τ_3^{-1}) in the strained condition, contrasting with their highest values in the unstrained case. This unusual behavior can be attributed to the changes in the ZA mode dispersion characteristics with strain. The application of strain diminishes the quadratic character while enhancing the linear character in the ZA mode dispersion. The transition of the ZA phonon dispersion from quadratic to linear results in a significant decrease in the population density of low-energy phonons. Consequently, the phase space corresponding to the four-phonon processes, in general, and involving ZA phonons, in particular, decreases. Based on these results, one can intuitively guess the role of four-phonon scattering in bulk-MoS_2 as well. In bulk-MoS_2, while the a-o frequency gap remains unchanged, the ZA phonon dispersion undergoes significant changes [48]. Due to the interlayer interaction, the ZA mode is split into the ZA and ZO′ modes. Additionally, the ZA phonon dispersion in bulk-MoS_2 exhibits a large reduction in its quadratic character compared to ML-MoS_2. As a result, the population density of the low-frequency ZA phonons reduces significantly in bulk-MoS_2, leading to a reduction in the four-phonon scattering strength. Similar phenomenon, manifesting a decrease in scattering phase space due to a reduction in phonon population density resulting from a transition from monolayer to bulk, have also been observed in graphene [30]. It is, therefore, evident that merely possessing the a-o frequency gap, reflection symmetry, and strong anharmonicity does not ensure a significant four-phonon scattering strength. The observations also indicate a strong coupling between the dispersion characteristics of the ZA mode and the corresponding four-phonon scattering strength of ML-MoS_2.

IV. CONCLUSIONS

In summary, using first-principles calculations we have demonstrated that the four-phonon scattering rate is surprisingly high in ML-MoS_2. Owing to the quadratic dependency of τ_4^{-1} on temperature, the four-phonon scattering strength becomes even higher and thus, dominates the overall phonon scattering processes at high temperatures. This disparity between the unusually high τ_4^{-1} and the relatively low τ_3^{-1} arises due to the restricted three-phonon phase space, resulting from the combined effects of the acoustic-optical frequency gap, strong anharmonicity and the presence of reflection symmetry in ML-MoS_2. The incorporation of four-phonon scattering in the thermal transport calculations leads to a significant reduction in the lattice thermal conductivity (κ_L) of ML-MoS_2. The discrepancy between the computed κ_L and the experimental data decreases from approximately 230% when only τ_3^{-1} is considered to about 30% when both τ_3^{-1} and τ_4^{-1} are taken into account. Additionally, we have identified that due to the significant presence of the Normal (N) scattering processes in ML-MoS2, the relaxation time approximation (RTA) results in an underestimation of κ_L. We, therefore, conjecture that employing an iterative scheme (IS) for both three- and four-phonon processes will yield the most accurate prediction of κ_L for ML-MoS_2. We observed that the κ_L associated with the acoustic phonon modes, in general, and the ZA mode, in particular, is significantly overestimated when only three-phonon scattering is taken into account. Furthermore, the importance of the quadratic dispersion of the ZA phonon branch and the resulting high population density of the low-energy ZA phonons, in driving the strong four-phonon scattering, is revealed through strained lattice calculations. ML-MoS_2, in the strained condition, despite meeting the necessary conditions for significant τ_4^{-1}, exhibits surprisingly low strength of four-phonon scattering. The results, thus, provide a critical revisit to the prevailing theories regarding the thermal transport properties of ML-MoS_2 and any other 2D TMDCs with analogous geometrical and phonon characteristics. Our work, thereby, significantly advances the first-principles based thermal transport calculations, enabling accurate prediction of thermal conductivity and offering a deeper understanding of the heat transport mechanism of ML-MoS_2.

ACKNOWLEDGMENTS

The first-principles calculations have been performed using the supercomputing facility of IIT Kharagpur established under the National Supercomputing Mission (NSM), Government of India and supported by the Centre for Development of Advanced Computing (CDAC), Pune. A.B. acknowledges SERB POWER Grant No. (SPG/2021/003874) and BRNS regular Grant No. (BRNS/37098) for the financial assistance. S.C. acknowledges MHRD, India, for financial support.

[1] B. Radisavljevic, M. B. Whitwick, and A. Kis, Integrated circuits and logic operations based on single-layer MoS_2, ACS Nano **5**, 9934 (2011).

[2] Q. H. Wang, K. Kalantar-Zadeh, A. Kis, J. N. Coleman, and M. S. Strano, Electronics and optoelectronics of two-dimensional transition metal dichalcogenides, Nat. Nanotechnol. **7**, 699 (2012).

[3] P. Johari and V. B. Shenoy, Tunable dielectric properties of transition metal dichalcogenides, ACS Nano **5**, 5903 (2011).

[4] D. Rai, T. V. Vu, A. Laref, M. A. Hossain, E. Haque, S. Ahmad, R. Khenata, and R. Thapa, Electronic properties and low lattice thermal conductivity (κ_l) of mono-layer (ML) MoS_2: FP-LAPW incorporated with spin–orbit coupling (SOC), RSC Adv. **10**, 18830 (2020).

[5] S. Chaudhuri, A. Bhattacharya, A. K. Das, G. P. Das, and B. N. Dev, Strain driven anomalous anisotropic enhancement in the thermoelectric performance of monolayer MoS_2, Appl. Surf. Sci. **626**, 157139 (2023).

[6] S.-D. Guo, Biaxial strain tuned thermoelectric properties in monolayer $PtSe_2$, J. Mater. Chem. C **4**, 9366 (2016).

[7] S. Chaudhuri, A. Bhattacharya, A. K. Das, G. P. Das, and B. N. Dev, Hydrostatic pressure induced anomalous enhancement in the thermoelectric performance of monolayer MoS_2, ACS Appl. Energy Mater. **6**, 11694 (2023).

[8] H. Wang, Y.-S. Lan, B. Dai, X.-W. Zhang, Z.-G. Wang, and N.-N. Ge, Improved thermoelectric performance of monolayer HfS_2 by strain engineering, ACS Omega **6**, 29820 (2021).

[9] J. Bera and S. Sahu, Strain induced valley degeneracy: a route to the enhancement of thermoelectric properties of monolayer WS_2, RSC Adv. **9**, 25216 (2019).

[10] S. Bhattacharyya, T. Pandey, and A. K. Singh, Effect of strain on electronic and thermoelectric properties of few layers to bulk MoS_2, Nanotechnology **25**, 465701 (2014).

[11] W. Huang, X. Luo, C. K. Gan, S. Y. Quek, and G. Liang, Theoretical study of thermoelectric properties of few-layer MoS_2 and WSe_2, Phys. Chem. Chem. Phys. **16**, 10866 (2014).

[12] J. Xiang, R. N. Ali, Y. Yang, Z. Zheng, B. Xiang, and X. Cui, Monolayer MoS_2 thermoelectric properties engineering via strain effect, Physica E **109**, 248 (2019).

[13] W. Li, J. Carrete, and N. Mingo, Thermal conductivity and phonon linewidths of monolayer MoS_2 from first principles, Appl. Phys. Lett. **103**, 253103 (2013).

[14] M. Sharma, A. Kumar, and P. Ahluwalia, Electron transport and thermoelectric performance of defected monolayer MoS_2, Physica E **107**, 117 (2019).

[15] X. Gu and R. Yang, Phonon transport in single-layer transition metal dichalcogenides: A first-principles study, Appl. Phys. Lett. **105**, 131903 (2014).

[16] A. N. Gandi and U. Schwingenschlögl, Thermal conductivity of bulk and monolayer MoS_2, Europhys. Lett. **113**, 36002 (2016).

[17] R. Yan, J. R. Simpson, S. Bertolazzi, J. Brivio, M. Watson, X. Wu, A. Kis, T. Luo, A. R. Hight Walker, and H. G. Xing, Thermal conductivity of monolayer molybdenum disulfide obtained from temperature-dependent Raman spectroscopy, ACS Nano **8**, 986 (2014).

[18] S. Sahoo, A. P. Gaur, M. Ahmadi, M. J.-F. Guinel, and R. S. Katiyar, Temperature-dependent Raman studies and thermal conductivity of few-layer MoS_2, J. Phys. Chem. C **117**, 9042 (2013).

[19] A. Krishnamoorthy, P. Rajak, P. Norouzzadeh, D. J. Singh, R. K. Kalia, A. Nakano, and P. Vashishta, Thermal conductivity of MoS_2 monolayers from molecular dynamics simulations, AIP Adv. **9**, 035042 (2019).

[20] X. Wei, Y. Wang, Y. Shen, G. Xie, H. Xiao, J. Zhong, and G. Zhang, Phonon thermal conductivity of monolayer MoS_2: A comparison with single layer graphene, Appl. Phys. Lett. **105**, 103902 (2014).

[21] Z. Ding, J.-W. Jiang, Q.-X. Pei, and Y.-W. Zhang, In-plane and cross-plane thermal conductivities of molybdenum disulfide, Nanotechnology **26**, 065703 (2015).

[22] Y. Cai, J. Lan, G. Zhang, and Y.-W. Zhang, Lattice vibrational modes and phonon thermal conductivity of monolayer MoS_2, Phys. Rev. B **89**, 035438 (2014).

[23] B. Peng, H. Zhang, H. Shao, Y. Xu, X. Zhang, and H. Zhu, Thermal conductivity of monolayer MoS_2, $MoSe_2$, and WS_2: interplay of mass effect, interatomic bonding and anharmonicity, RSC Adv. **6**, 5767 (2016).

[24] D. A. Broido, M. Malorny, G. Birner, N. Mingo, and D. Stewart, Intrinsic lattice thermal conductivity of semiconductors from first principles, Appl. Phys. Lett. **91**, 231922 (2007).

[25] J. Garg, N. Bonini, B. Kozinsky, and N. Marzari, Role of disorder and anharmonicity in the thermal conductivity of silicon-germanium alloys: A first-principles study, Phys. Rev. Lett. **106**, 045901 (2011).

[26] W. Li, N. Mingo, L. Lindsay, D. A. Broido, D. A. Stewart, and N. A. Katcho, Thermal conductivity of diamond nanowires from first principles, Phys. Rev. B **85**, 195436 (2012).

[27] W. Li, L. Lindsay, D. A. Broido, D. A. Stewart, and N. Mingo, Thermal conductivity of bulk and nanowire $Mg_2Si_xSn_{1-x}$ alloys from first principles, Phys. Rev. B **86**, 174307 (2012).

[28] T. Feng and X. Ruan, Quantum mechanical prediction of four-phonon scattering rates and reduced thermal conductivity of solids, Phys. Rev. B **93**, 045202 (2016).

[29] T. Feng, L. Lindsay, and X. Ruan, Four-phonon scattering significantly reduces intrinsic thermal conductivity of solids, Phys. Rev. B **96**, 161201(R) (2017).

[30] T. Feng and X. Ruan, Four-phonon scattering reduces intrinsic thermal conductivity of graphene and the contributions from flexural phonons, Phys. Rev. B **97**, 045202 (2018).

[31] X. Yang, T. Feng, J. Li, and X. Ruan, Stronger role of four-phonon scattering than three-phonon scattering in thermal conductivity of III-V semiconductors at room temperature, Phys. Rev. B **100**, 245203 (2019).

[32] Y. Zhang, Z. Tong, A. Pecchia, C. Yam, T. Dumitrică, and T. Frauenheim, Four-phonon and electron–phonon scattering effects on thermal properties in two-dimensional 2H-TaS_2, Nanoscale **14**, 13053 (2022).

[33] L. Lindsay, D. A. Broido, and N. Mingo, Flexural phonons and thermal transport in graphene, Phys. Rev. B **82**, 115427 (2010).

[34] S. Chaudhuri, A. K. Das, G. P. Das, and B. N. Dev, Strain induced effects on the electronic and phononic properties of 2H and 1T monolayer MoS_2, Phys. B: Condens. Matter **655**, 414701 (2023).

[35] S. Chaudhuri, A. K. Das, G. P. Das, and B. N. Dev, *Ab initio* study of electronic and lattice dynamical properties of monolayer ZnO under strain, J. Electron. Mater. **52**, 1633 (2023).

[36] G. Kresse and J. Furthmüller, Efficient iterative schemes for *ab initio* total-energy calculations using a plane-wave basis set, Phys. Rev. B **54**, 11169 (1996).

[37] G. Kresse and J. Furthmüller, Efficiency of *ab initio* total energy calculations for metals and semiconductors using a plane-wave basis set, Comput. Mater. Sci. **6**, 15 (1996).

[38] G. Kresse and D. Joubert, From ultrasoft pseudopotentials to the projector augmented-wave method, Phys. Rev. B **59**, 1758 (1999).

[39] J. P. Perdew, K. Burke, and M. Ernzerhof, Generalized gradient approximation made simple, Phys. Rev. Lett. **77**, 3865 (1996).

[40] H. J. Monkhorst and J. D. Pack, Special points for Brillouin-zone integrations, Phys. Rev. B **13**, 5188 (1976).

[41] A. Togo and I. Tanaka, First principles phonon calculations in materials science, Scr. Mater. **108**, 1 (2015).

[42] W. Li, J. Carrete, N. A. Katcho, and N. Mingo, SHENGBTE: A solver of the Boltzmann transport equation for phonons, Comput. Phys. Commun. **185**, 1747 (2014).

[43] G. D. Mahan, *Many-Particle Physics* (Springer Science & Business Media, 2000).

[44] N. Jena, A. De Sarkar *et al.*, Compressive strain induced enhancement in thermoelectric-power-factor in monolayer MoS_2 nanosheet, J. Phys.: Condens. Matter **29**, 225501 (2017).

[45] L. Zhu, W. Li, and F. Ding, Giant thermal conductivity in diamane and the influence of horizontal reflection symmetry on phonon scattering, Nanoscale **11**, 4248 (2019).

[46] See Supplemental Material at http://link.aps.org/supplemental/10.1103/PhysRevB.109.235424 for the variation in three- and four-phonon scattering rates with temperature at the q-point (0.3, 0, 0), the scattering rates corresponding to all possible three- and four-phonon processes as well as corresponding to the Normal and Umklapp processes for both the unstrained and strained conditions.

[47] Z. Ding, Q.-X. Pei, J.-W. Jiang, and Y.-W. Zhang, Manipulating the thermal conductivity of monolayer MoS_2 via lattice defect and strain engineering, J. Phys. Chem. C **119**, 16358 (2015).

[48] H. Tornatzky, R. Gillen, H. Uchiyama, and J. Maultzsch, Phonon dispersion in MoS_2, Phys. Rev. B **99**, 144309 (2019).